ARMY RESEARCH LABORATORY

Global Mechanical Response and Its Relation to Deformation and Failure Modes at Various Length Scales Under Shock Impact in Alumina AD995 Armor Ceramic

by D. P. Dandekar, J. W. McCauley, W. H. Green, N. K. Bourne, and M. W. Chen

ARL-RP-202 **March 2008**

A reprint from the *25th Army Science Conference*, Orlando, FL, 27–30 November 2006.

NOTICES

Disclaimers

The findings in this report are not to be construed as an official Department of the Army position unless so designated by other authorized documents.

Citation of manufacturer's or trade names does not constitute an official endorsement or approval of the use thereof.

Destroy this report when it is no longer needed. Do not return it to the originator.

Army Research Laboratory
Aberdeen Proving Ground, MD 21005-5069

ARL-RP-202 **March 2008**

Global Mechanical Response and Its Relation to Deformation and Failure Modes at Various Length Scales Under Shock Impact in Alumina AD995 Armor Ceramic

D. P. Dandekar, J. W. McCauley, and W. H. Green
Weapons and Materials Research Directorate, ARL

N. K. Bourne
University of Manchester

M. W. Chen
Johns Hopkins University and Tohoku University

A reprint from the *25th Army Science Conference*,
Orlando, FL, 27–30 November 2006.

REPORT DOCUMENTATION PAGE	Form Approved OMB No. 0704-0188

1. REPORT DATE *(DD-MM-YYYY)*	2. REPORT TYPE	3. DATES COVERED (From - To)
March 2008	Reprint	January 2003–December 2006

4. TITLE AND SUBTITLE
Global Mechanical Response and Its Relation to Deformation and Failure Modes at Various Length Scales Under Shock Impact in Alumina AD995 Armor Ceramic

5a. CONTRACT NUMBER

5b. GRANT NUMBER

5c. PROGRAM ELEMENT NUMBER

6. AUTHOR(S)
D. P. Dandekar, James W. McCauley, W. H. Green, N. K. Bourne,[*] and M. W. Chen[†]

5d. PROJECT NUMBER
AH42 and AH43 and BH64

5e. TASK NUMBER

5f. WORK UNIT NUMBER

7. PERFORMING ORGANIZATION NAME(S) AND ADDRESS(ES)
U.S. Army Research Laboratory
ATTN: AMSRD-ARL-WM-TD
Aberdeen Proving Ground, MD 21005-5069

8. PERFORMING ORGANIZATION REPORT NUMBER
ARL-RP-202

9. SPONSORING/MONITORING AGENCY NAME(S) AND ADDRESS(ES)

10. SPONSOR/MONITOR'S ACRONYM(S)

11. SPONSOR/MONITOR'S REPORT NUMBER(S)

12. DISTRIBUTION/AVAILABILITY STATEMENT
Approved for public release; distribution is unlimited.

13. SUPPLEMENTARY NOTES
A reprint from the *25th Army Science Conference*, Orlando, FL, 27–30 November 2006.
[*]University of Manchester, United Kingdom
[†]Johns Hopkins University, Baltimore, MD, and Tohoku University, Sendai, Japan

14. ABSTRACT
Polycrystalline aluminum oxide (Al_2O_3) based materials have both personnel and ground vehicle armor applications. However, their ballistic performance can vary significantly. At the root of this problem is the identification of the fundamental macro and micro mechanisms of deformation and failure in the ballistic event which has proven very elusive over the years. Using a newly developed soft recovery plate impact experiment, a multi-disciplinary, multi-national collaboration has, for the first time, determined micro and macro deformation and damage mechanism maps relating the experimentally measured global mechanical response of a material through matured shock wave diagnostics to the nature of concurrent deformation and damage generated at varying length scales under shock wave loading.

15. SUBJECT TERMS
armor ceramics, shock impact, alumina characterization, Hugoniot elastic limit, twinning

16. SECURITY CLASSIFICATION OF:			17. LIMITATION OF ABSTRACT	18. NUMBER OF PAGES	19a. NAME OF RESPONSIBLE PERSON
a. REPORT	b. ABSTRACT	c. THIS PAGE			D. P. Dandekar
UNCLASSIFIED	UNCLASSIFIED	UNCLASSIFIED	UL	18	19b. TELEPHONE NUMBER (*Include area code*) 410-306-0711

GLOBAL MECHANICAL RESPONSE AND ITS RELATION TO DEFORMATION AND FAILURE MODES AT VARIOUS LENGTH SCALES UNDER SHOCK IMPACT IN ALUMINA AD995 ARMOR CERAMIC

D. P. Dandekar*, J. W. McCauley, and W. H. Green
Army Research Laboratory, APG, MD 21005

N. K. Bourne
University of Manchester, UK

M. W. Chen
Johns Hopkins University, Baltimore MD and Tohoku University, Sendai, Japan

ABSTRACT

Polycrystalline aluminum oxide (Al_2O_3) based materials have both personnel and ground vehicle armor applications. However, their ballistic performance can vary significantly. At the root of this problem is the identification of the fundamental macro and micro mechanisms of deformation and failure in the ballistic event which has proven very elusive over the years. Using a newly developed soft recovery plate impact experiment, a multi-disciplinary, multi-national collaboration has, for the first time, determined micro and macro deformation and damage mechanism maps relating the experimentally measured global mechanical response of a material through matured shock wave diagnostics to the nature of concurrent deformation and damage generated at varying length scales under shock wave loading.

1. INTRODUCTION

Current operations in Iraq and Afghanistan unambiguously demonstrate the need for threat specific, reduced weight, transparent and opaque armor in many army systems, including personnel protection. As the threats have escalated and become more varied, the challenges for rapidly developing optimized threat specific armor packages have grown complex. Certain high performance structural ceramics, Al_2O_3, B_4C, SiC, TiB_2, AlN, AlON, spinel, glass, etc. have proven to be effective armor materials at much lower weights in many systems. A critical key to further accelerating optimization of these materials is development of validated predictive performance computer models. This approach is based on the determination and quantification of the various ballistic energy absorption mechanisms, including the various deformation modes, damage nucleation and accumulation processes, and the resulting eventual failure of armor ceramics at high rates under very high impact stress (shock wave), comparable to the ballistic event.

Polycrystalline aluminum oxide (Al_2O_3 - alumina), known as sapphire in single crystal form, has been used for many years in both personnel and ground vehicle armor applications. Yet the ballistic performance of alumina based armor ceramic materials can vary significantly, a major challenge for systematic material optimization, valid simulation, prediction, and design of armor systems. We seek to address this problem through identification of the fundamental mechanisms of deformation and failure of alumina in the ballistic event.

Past efforts have used instrumented laboratory high strain rate/high pressure mechanical tests including Split Hopkinson Pressure Bar (SHPB/ Kolsky Bar) and plate impact (shock wave) to mimic, in a controlled environment, the response of armor materials under ballistic high strain rate – high stress conditions. But there are two major problems associated with this approach: (A) recovery of samples from the test suitable for detailed characterization, and (B) identification of the deformation and failure mechanisms that cut across length scales from centimeters to nanometers. This has been a major challenge over the years.

Using a newly developed soft recovery technique (Bourne et. al. 2006), an international team drawn from the Army Research Laboratory (ARL), Royal Military College of Science (RMCS), Shrivenham, UK, the University of Manchester, Manchester, UK, Johns Hopkins University and Tohoku University, Sendai, Japan, focused on AD995 (CoorsTek, Co.), a very well known commercial high purity alumina. This collaboration has, for the first time, determined micro and macro deformation and damage mechanism maps that relate the experimentally measured global mechanical response of a material through matured shock wave diagnostics to the nature of concurrent deformation and damage generated at varying scales under shock wave loading. These results can provide a critical missing link in the development of better physical material models and materials.

2. MATERIAL

AD995 is composed of polycrystalline aluminum oxide (Al_2O_3) and aluminosilicate glass. It contains 99.5% aluminum oxide. The measured density of AD995 is 3.880 ± 0.003 Mg/m^3. Theoretical density of such a material should be 3.96 Mg/m^3. The difference is attributed to the presence of a glassy phase and pores/voids in the material [Figure 1]. Ultrasonic longitudinal and shear wave velocities are 10.56 ± 0.03, and 6.25 ± 0.08 km/s, respectively (Dandekar and Bartkowski 1994).

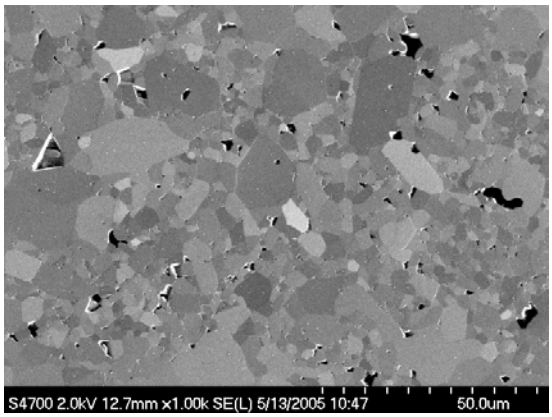

Figure 1. SEM of AD995 (M. Motyka, ARL).

3. EXPERIMENTAL METHODS

Three independent sets of experiments were performed to determine: (i) the shock wave response of AD995 under compression (to 18 GPa), and subsequent release, and tension to determine global compressibility, shear and spall (tensile) strengths using piezo-resistive gages and velocity interferometer (VISAR) under a single shock, (ii) the response of AD995 under repeated shock wave compression and subsequent releases to 10.5 GPa, and (iii) the nature of deformation on meso to nm scale from shock recovered AD995.

Shock wave experiments were performed on 10 and 5 cm diameter single stage light gas guns at ARL and RMCS, respectively to determine compression, shear and tensile/spall strengths of AD995. Experiments under two successive shocks were done at ARL to determine the change in compressibility and shear strength of AD995 due to propagation of the first shock wave. Shock recovery experiments were performed at RMCS. Readers are referred to Dandekar and Bartkowski (1994), Dandekar (2001), Cooper et al. (2006), and Bourne et al. (2006) for the design, configuration, and diagnostic details of these experiments[1].

These experiments were carried out in the stress regimes where AD995 deformed globally in elastic manner and the regime where AD995 deformed inelastically. The boundary between these two regimes is nominally called the Hugoniot Elastic Limit (HEL) [Figure 2]. The HEL of AD995 is 6.7 GPa. Shock recovery experiments on AD995 were performed at 4, 6, and 7.8 GPa, i.e., the stress regime where AD995 deforms globally as an elastic solid and an elastic-plastic solid. Shock recovered specimens of AD995 were examined under optical microscopy (OM), X-ray computed tomography (XCT), Field Emission Scanning Electron Microscopy (SEM) and, Transmission Electron Microscopy (TEM) to determine details of shock wave induced deformation in the material i.e., the nature of deformation of AD995 at different length scales. Resolutions of OM, and XCT vary from microns to mm, while the resolution of SEM and TEM vary between few nm to a few microns. The results of these shock wave experiments permit us to link the observed global deformation of AD995 to deformation at various length scales below and above the HEL

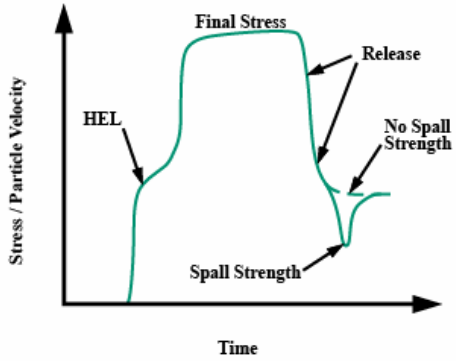

Figure 2. Idealized shock wave profile in elastic-inelastic material. Final stress corresponds to the inelastic stress in the material.

OM and XCT characterizations of shock recovered specimens were done at ARL. SEM and TEM characterizations of the recovered AD995 were done at Johns Hopkins University, Maryland and Tohoku University, Japan.

4. SHOCK RESPONSE OF AD995

Shock wave experiments, when appropriately designed, yield values of mechanical properties i.e., compressibility, shear and the tensile/spall strengths as a function of stress. The stress (σ)- volume ratio (V/V_0), where V_0 is the initial volume, defines the Hugoniot of a material (Fig. 3). The compression from Equation of State is hydrodynamic or mean stress compression of the material. The magnitude of shear strength may be calculated in two ways: either from the difference between the shock hugoniot stress, σ (V/V_0), and the

[1] Page limitation does not permit us to give details of these experiments.

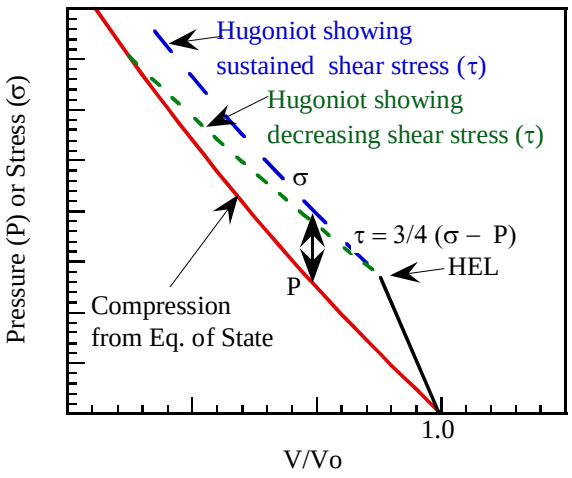

Figure 3. A schematic of shock Hugoniot and hydrodynamic compression of a solid material.

hydrodynamic pressure, $P(V/V_0)$, at given compression (V/V_0) or from the concurrent measurements of the Hugoniot stress and lateral stress at a given compression. A schematic of the compressive behavior of a material under hydrodynamic compression and plane shock wave compression is shown in Fig. 3. The value of the shear strength $[\tau\ (V/V_0)]$ at a given compression is given by:

$$\tau = 0.75[\sigma(V/V_0) - P(V/V_0)] \qquad (1)$$

And from lateral stress (σ_y) measurements, the value of shear strength is obtained from

$$\tau = 0.5[\ \sigma(V/V_0) - \sigma_y\ ] \qquad (2)$$

Thus the shear strength determined is independent of any assumption about the nature of the inelastic deformation of the material. Fig. 3 shows trends in the magnitudes of shear strength as a function of impact/Hugoniot stress for materials which do not suffer a loss of shear strength ($\tau > 0$) and those which do ($\tau \to 0$).

Spall strength of material is obtained from the difference in the magnitude of stress between Final stress and Spall strength shown in Fig. 2.

Figures 4 and 5 show a few representative shock wave profiles recorded in compression-spall and lateral stress experiments performed on AD995, respectively. Fig. 4 shows that plastic wave is not fully developed when AD995 is shocked to 11.1 GPa although the HEL, as indicated by the break in the slope of the wave profiles, is clearly seen recorded at 8.4 and 11.1 GPa. The Hugoniot Elastic Limit (HEL) of AD995 is found to be 6.71±0.08 GPa. The tensile/spall strength of AD995 declines with an increase in the magnitude of shock

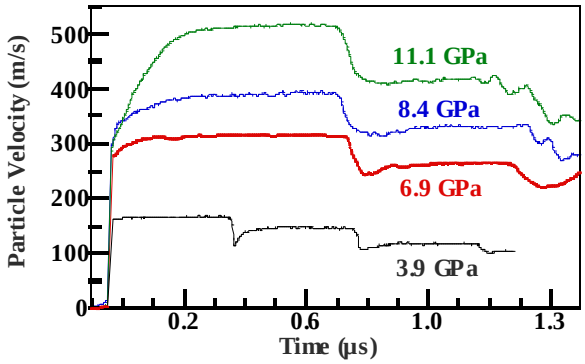

Figure 4. Shock wave profiles in AD995.

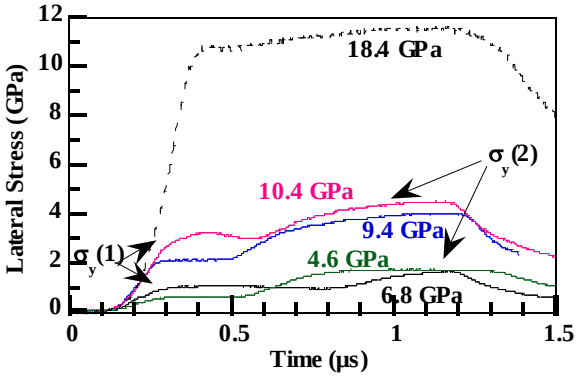

Figure 5. Lateral stress profiles in AD995

induced stress ultimately vanishing between 8.4 and 11.1 GPa.

Elastic Compression

Dandekar and Bartkowski (1994) reported the Hugoniot Elastic Limit (HEL) of AD995 to be 6.67 ± 0.24 GPa. Grady (Personal communication) reported a value of 6.5 GPa for the HEL of AD995. Dandekar (2001) performed double shock experiments on AD995 to probe the nature of deformation of AD995 at 6.8 and 10.4 GPa. Dandekar found that both the amplitudes and widths of the stress wave profiles in AD995 due to first and second shock with their respective releases are identical when shocked to 6.78 ± 0.17 GPa. Ewart and Dandekar (1994) showed that with the currently used diagnostic in shock wave experiments it is not possible to detect a small volume change, i.e. compressibility of a material under shock wave propagation due to pore closure or generation and growth of small number of cracks and their lengths. The compression duration of the first and second shock wave was 0.37 μs. The second shock propagated in AD995 after the stress generated by the first shock was totally released. This result implied that global and dominant deformation of AD995 at 6.78 GPa was elastic and reversible i.e., the stress and strain states were attained through elastic deformation. The associated values of density and particle velocity at the

HEL are 3.940 ± 0.004 Mg/m^3 and 0.162 ± 0.005 km/s, respectively. Reinhart and Chabbildas (2003) report values of HEL varying from 6.7 to 7.89 GPa.

Inelastic Compression

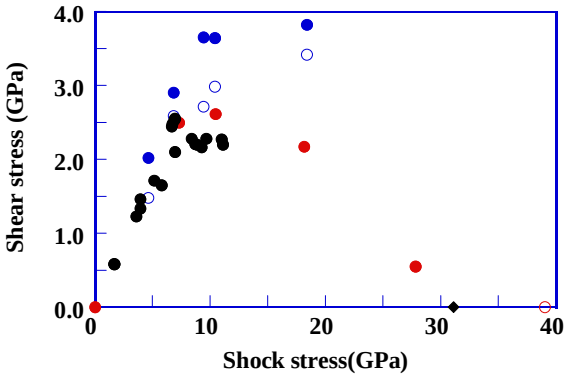

Figure 6. Shear stress sustained in AD995 with shock induced stress. solid and hollow symbols; RED: Grady (Personal communication) and, Reinhart and Chhabildas (2003), Blue: Cooper et al. (2006), Black Dandekar and Bartkowski (1994).

Fig. 6 shows the variation in the value of shear stress sustained in AD995 as function of shock induced stress. Results obtained by Dandekar and Bartkowski (1994) and by Grady (Personal communication) from the offset between the shock Hugoniot and hydrodynamic compression suggest that deformation of AD995 above its HEL is elastic-plastic to around 12 GPa. Above 12 GPa, AD995 begins to possess a decreasing magnitude of shear strength with an increase in shock stress. However, the results of lateral stress measurements indicate AD995 continues to maintain increasing shear strength to 18.5 GPa. Shock data of Grady show that AD995 suffers a total loss of shear strength around 31 GPa. Reinhart and Chabbildas (2003) found that AD995 has no shear strength at and above 39 GPa. The discrepancy in the shear strength values of AD995 obtained from the offset between the shock Hugoniot and hydrodynamic compression and lateral stress measurement remains to be resolved. However, the discrepancy does not impact the results of the current work dealing with the determination of nature of deformation from the existing shock wave data and features observed in the of shock recovered AD995 by means of optical microphotography (OM), X-ray computed tomography (XCT) and, transmission electron microscopy (TEM).

Spall Strength

Spall strength of AD995 is impulse dependent (Table 1). For instance, at the HEL, 6.7 GPa, of AD995, the values of spall strengths are 0.31, 0.37, and 0.45 GPa for compressive pulse durations/pulse width of approximately 0.70, 0.35, and 0.16 μs respectively. The dependence of spall strength on the pulse width is evident even when AD995 is shocked to as low as 1.7 GPa or as high as 9.27 GPa. In general, spall strength of AD995 decreases with an increase in both the magnitudes of shock compressive stress and their durations. For example, spall strength declines from a value of 0.46 GPa to 0.295 GPa at shock induced stress of 1.7 GPa and 8.2 GPa for a pulse width of around 0.7 μs. Spall strength vanishes at 8.8 GPa for a pulse width of 0.7 μs. The decrease in the value of spall strength at and below the HEL irrespective of the pulse widths between 0.16 and 0.7 μs suggests an increase in the population of micro-cracks in AD995 under shock compression and release even when shocked to as low as 1.7 GPa prior to generation of tensile stress as a result of release wave interaction in AD995. Diminution of the spall strength of AD995 is attributed to dominant brittle character of AD995.

TABLE 1. AD995 Spall Strength .

Shot #	Impact Velocity (km/s)	Pulse Width (μs)	Impact Stress (GPa)	Spall Strength (GPa)
213	0.0829	0.743	1.70	0.458
307	0.0780	0.369	1.67	0.612
240	0.175	0.720	3.79	0.387
303	0.182	0.354	3.91	0.568
234	0.251	0.687	5.36	0.421
329	0.295	0.783	5.69	0.357
224	0.349	0.699	6.94	0.306
313	0.323	0.349	6.93	0.367
314	0.320	0.165	6.71	0.456
331	0.313	0.165	6.49	0.476
229	0.433	0.694	8.35	0.295
304	0.465	0.671	8.82	-
309	0.418	0.342	8.63	0.331
236	0.512	0.709	9.53	-
310	0.450	0.338	9.27	0.247
301	0.597	0.702	10.84	-
239	0.604	0.697	11.04	-

5. SHOCK RECOVERED AD995

Design of shock recovery experiments ensured that AD995 specimen was subjected to a single shock wave compressive stress of a predetermined magnitude followed by release of the compressive stress before the effects of lateral stress release distorted the compressive and release histories especially in the central region of the AD995 specimen. Further, the design ensured that no tension developed in AD995 due to wave interactions. Thus the observed features in the recovered AD995 could be unambiguously associated with the shock induced planer shock compression and release.

Optically Observed Features: scale 1mm – 1 cm

Photographs of the three sets of samples in their brass holders are shown in Figure 7. Figure 8 shows the macro-crack pattern of damage observed in the recovered, centrally sectioned and dye penetrated alumina discs. The sectioned surface of the disc that was subjected to the 4 GPa shock was coated with a transparent resin, which alters its fractographs. Broadly, the network of macrocracks consists of horizontal and vertical fissures, resulting in numerous fractured material blocks populating the specimen volume. The specimens subjected to the higher shock stresses show marked evidence of a higher macrocrack density in the central region. Fracture planes that traverse the entire specimen width are also seen in Figure 8, and notably, a fracture cavity is present on the impact surface of the specimen subjected to a shock compression of 7.8 GPa. However, it is difficult to asses the volume occupied by the cracks at these stresses. The population and size of macro-cracks does help to understand the observed decrement of spall strength of AD995 with increase in the magnitude of shock induced stress and its duration.

Figure 7. Recovered samples in brass holders.

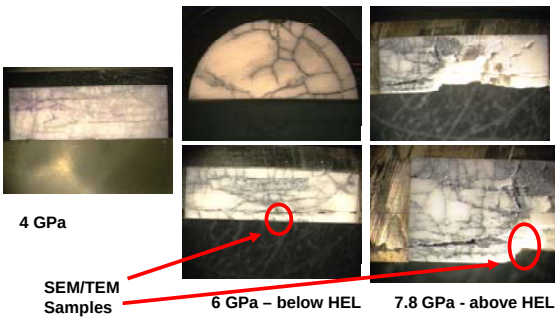

Figure 8. Optical Microscopy of Stained fracture patterns in cross section and top view (6 GPa)

X-ray Computed Tomography: scale 0.1 mm – 1 cm:

X-ray computed tomography (XCT) may be applied to any material through which a beam of penetrating radiation may be passed and detected, including metals, plastics, ceramics, metallic/non-metallic composite material, and assemblies. The principal advantage of XCT is that it provides densitometric images of thin cross sections through an object. Because of the absence of structural superimposition, images are easier to interpret than conventional radiological images. Further, because XCT images are digital, the images may be enhanced, analyzed, compressed, archived, input as data to performance calculations, compared with digital data from non-destructive evaluation modalities, or transmitted to other locations for remote viewing, or a combination thereof.

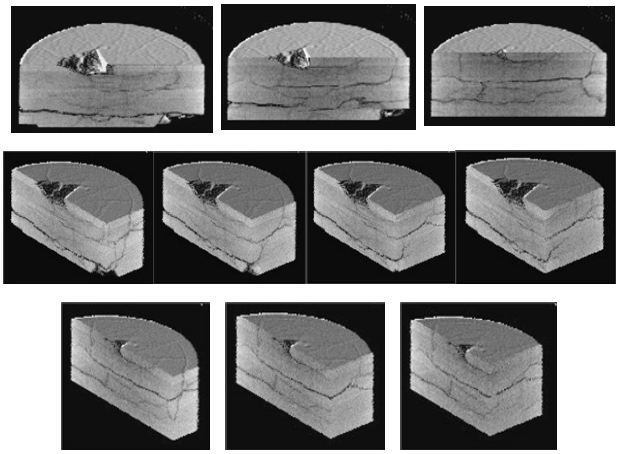

Figure 9. Three-Dimensional (3-D) virtual solid images of 6 GPa sample with sections cut away

A sectioned half-disk from each recovered sample was inspected using a customized XCT system (scanner) at the U.S. Army Research Laboratory (ARL). It has a 420 keV X-ray tube with two focal spot sizes and a 225 keV microfocus X-ray tube with a variable focal spot size down to 5 μm. A dedicated embedded industrial computer system controls object scanning (*i.e.* data collection) and image reconstruction, viewing, and processing.

The sample was scanned parallel to its faces, making the cross-sectional image plane perpendicular to the through thickness direction. Each sample was scanned from its impact side (in contact with the cover plate) to its rear face. Each slice was reconstructed to a 1024 by 1024 image matrix collecting 3600 views (i.e. projections) during the full rotation and with about 60 slices required to completely scan each sample. The tube energy and current used were 160 keV and 0.035 mA, respectively, and the focal spot was 20 μm.

Bourne et al. (2006) describe, and present in detail, results of XCT scans done on the recovered specimen of shocked AD995 to 6 GPa. The excellent dimensional accuracy and the digital nature of XCT images allow the accurate volume reconstruction of multiple adjacent slices. Figure 9 shows a series of three –dimensional solid images of the 6 GPa sample with various sections virtually removed. The top three images are looking down at the sectioned side of the sample with it tilted 25^0 to the impact side: top left is just inside the actual surface, the next two are 1 and 2 mm from the actual

surface; the next four images have been rotated 50º about the z axis with the distances on the right from the corner being 2.3, 3.3, 4.4, 5.4 mm respectively; the last three images are similar to the previous four, but sectioned at closer to the edge of the sample, at 2.3, 4.4, and 6.4 mm form the actual sample corner.

A three-dimensional, reconstructed solid of the virtual damage distribution within the sample, in which the undamaged material is made partially transparent to view the damaged areas indicated in white, is shown in Fig.10. The impact side of the original sample in this view is below the sectioned face as indicated by the large white area on the bottom.

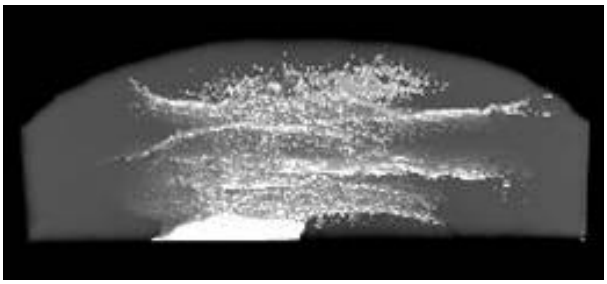

Figure 10. 3-D virtual solid of damage distribution

SEM and TEM Features: scale = 10 μm – 1 nm:

The deformation and failure mechanisms operating in shock-loaded AD995 alumina were systematically investigated by employing scanning electron microscopy (SEM) and transmission electron microscopy (TEM) [Chen et. al. 2006]. Two samples subjected to shock-induced stresses of 6.0 GPa and 7.8 GPa (below and above its HEL of 6.7 GPa) were separately sectioned and imaged (Fig. 8).

SEM observations suggest a transition in fracture behavior from intergranular-dominated fracture (at a stress of 6 GPa below the HEL) to cleavage-dominated (at 7.8 GPa above the HEL). Fig. 11 (a). shows a SEM micrograph taken from the 6 GPa sample. The fracture surface corresponds to individual grains with smooth facets, suggesting failure along grain boundaries (GBs). SEM micrographs of the fragment surfaces (see Fig. 12 (a) and (b) show failure of the 7.8 GPa specimen is dominated by transgranular fracture. Typical cleavage features including river patterns and cleavage steps along specific crystal directions, can be identified in Fig. 12(b).

A majority of grains in AD995, subjected to 6 GPa, did not exhibit plastic deformation on the facetted surfaces. Occasionally, dislocations can be found in the vicinity of grain boundaries as seen the bright-field TEM micrograph in Fig.11 (c). The dislocations and dislocation arrays most likely emitted from a grain boundary are characterized as normal dislocations.

Both SEM and TEM observations indicate that the 6.0 GPa specimen experienced mainly elastic deformation during shock loading. The limited plastic deformation in the vicinity of GBs found by systematic TEM characterization may be produced by localized stress concentrations arising from the propagation of GB cracks, defects at grain boundaries, or grain-to-grain elasticity mismatch, which promote the nucleation of the observed dislocation. Because concentrated stresses always degrade quickly from GBs, the generated dislocations may not be able to move too far from their sources at GBs, only resulting in local plastic deformation. Apparently, this localized plasticity cannot significantly affect the overall elastic response of the material to the applied shock loading.

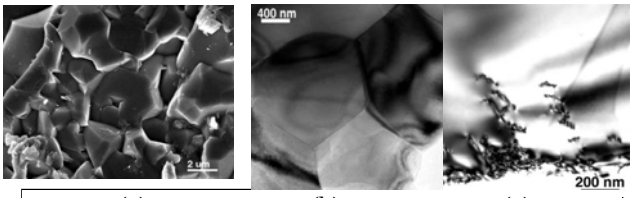

(a) (b) (c)

Figure 11. SEM and TEMs of 6 GPa sample: a.) SEM in uncracked area; b.) TEM in uncracked area and c.) TEM in cracked area

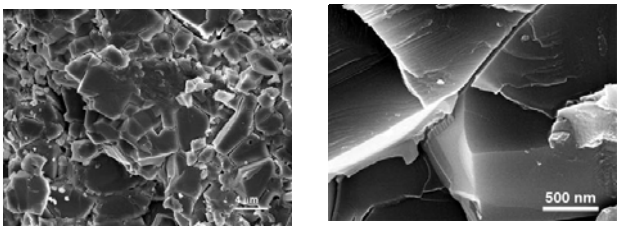

(a) (b)

Figure 12. SEMs of 7.8 GPa sample

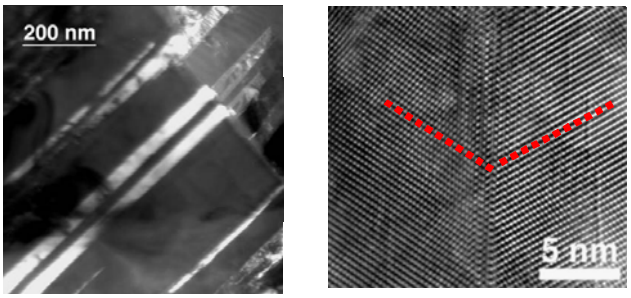

(a) (b)

Figure 13. TEMs of 7.8 GPa sample

Dramatic changes in the deformation mode behavior were found in the AD995 alumina specimen experiencing an impact pressure of 7.8 GPa. TEM characterization suggests that numerous deformation twins appear in a large number of grains as illustrated in Fig.13 (a) and (b). The twin bands in each grain parallel each other along a common crystallographic orientation, suggesting only one slip system was activated in each

grain during shock loading. In the dark-field TEM micrograph, twin dislocations can be identified within the twin bands. They were determined to be 1/3[1010] partial dislocations. High-resolution electron microscope (HREM) characterization shows that the width of the twin bands ranges from several to tens of nanometers (Fig.13 (a)) and the twin interfaces contain a large number of twinning dislocations [Figure 13(**b**)]. HREM image simulations suggest that the twinning is along the basal plane (0001) of the hexagonal unit cell. Thus, these deformation twins are determined to be the basal twins. The critical shear stress (τ_c) for the formation of deformation twins in perfect alumina crystals can be roughly estimated according to a simple equation (Hirth and Lothe, 1982).

$$\tau_C = \frac{\gamma}{b_P} \qquad (3)$$

where b_P is the magnitude of the Burgers vector of the twin dislocations and γ is the stacking fault energy. The estimated critical shear stress ranges from 5-8 GPa, which is in the same magnitude of the HEL of alumina (4~16 GPa) reported so far and very close to the one half of the HEL values of the polycrystalline alumina with high purity and density. This suggests that the twinning driven by the shear component of the uniaxial shock compression stress appears to be responsible for the elastic-to-inelastic transition at the

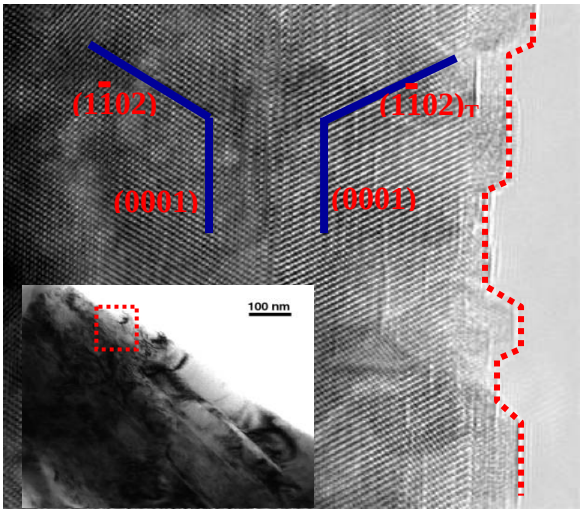

Figure 14. **.** Lattice image of a thin fragment. The facetted edge is mainly parallel to (0001) basal plane. The cleavage steps marked in the figure are either parallel to the matrix (1-102) plane or to the (1-102) plane of the twin band.

It is interesting to note (Fig.14) that the edges of the 7.8 GPa fragments are frequently facetted on (0001) twinning planes, indicating an intrinsic correlation between deformation twins and the cleavage failure**.** The HREM image taken from a recovered specimen exhibits a facetted edge that appears along an interface of the twin band shown in the lattice image. The edge is mainly along (0001) basal planes with steps parallel to (1-102) plane of either the matrix or the twin band, as indicated by the dashed line. The apparent cleavage along (0001) twin planes and the appearance of (1-102) planes of both twin and matrix as the cleavage steps, suggest that the fracture is along the interface of the twin bands during shock loading or unloading. It appears that the generation of deformation twins in the shock-loaded alumina provides a shortcut, or energetically more favorable path, for cleavage cracking and thereby a change in the fracture mode from intergranular behavior to transgranular cleavage.

It has been well known that shock, i.e. high rates of load application and release, favors twin formation in a number of materials, probably due to rate sensitive inertial effects. The process of twinning can form in time periods as short as a few microseconds, while for slip accomplished by normal dislocation gliding there is a delay time of several milliseconds before a slip band is produced. The slip process by dislocation gliding seems to be resistant to shock loading, that is, the movement of dislocations for appreciable distance requires that the stress is applied for a considerable time period. In crystals with high plastic slip resistance, such as ceramics, under uniform levels of stress, twins can propagate with near sonic velocity. Recent molecular dynamics simulations also suggest that dislocation motion at high strain rates become jagged, resulting in spontaneous self-pinning. Then, at still higher strain rates, the dislocation stops abruptly and emits a twin plate that immediately takes over as the dominant mode of plastic deformation. Twinning requires a high concentration of strain energy and this should be readily available during shock loading. The elastic strain energy stored during ramp up to the HEL will drive the twinning movements even after the passage of the shock wave when the time periods of shock loading is shorter than the twinning process. Cracking along twinning interfaces has been observed in a number of brittle materials and various explanations have been proposed. For the case of shock-loaded AD995 alumina, it is most likely that the cleavage along the twin boundaries is caused by the deviatoric stresses applied to the twin bands during unloading and the relative weak chemical bonding at the non-relaxed twinning interfaces.

6. DISCUSSION

The observations in this study provide compelling experimental evidence for the micromechanism responsible for shock induced global plastic deformation

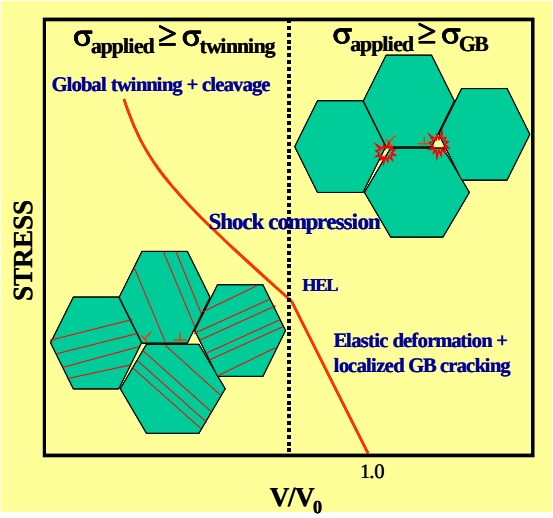

Figure 15. Schematics of the correlation of HEL with micro-plasticity and cracking, in which σ is shock stress, σ_{gb} is the cohesion of grain boundaries, and σ_{twin} is the critical stress for twinning.

in AD995 alumina. The HEL appears to be associated with the onset of deformation twinning, which drives the primary fracture mode from an intergranular one (below the HEL) to transgranular cleavage above HEL. The correlation of HEL with micro-plasticity and fracture can be represented in the schematic shown in Figure 15.

When the impact velocity is such that the induced stress is below HEL, deformation twins are not activated. However, it may be high enough to cause intergranular fracture and the formation of dislocations in the vicinity of GBs, seemingly produced by stress concentrations caused by GB crack propagation, existing GB flaws or grain-to-grain elasticity mismatch. Since they are localized and discontinuous, the cracking and dislocation gliding are not expected to significantly affect the overall primarily elastic response of the material as shown to be the case under compression and release. However, under shock generated tension, the deleterious effect of cracking is significant even at as low a stress as 1.7 GPa as evident from the pulse width dependence of the spall strength of AD995. At stresses greater than the HEL, the applied stresses are higher than the critical stresses for twinning. Thus, deformation twins can be activated in a large number of grains prior to the GB cracking. This global plastic deformation causes the inelastic response and the twining planes provide an easy means for cleavage fracture, giving rise to a change in the fracture morphology. Finally, the OM, XCT, SEM and TEM characterizations of the shock recovered AD995 provides an opportunity for modeling of the material at varying length scales to reproduce the shock response of AD995 obtained from shock wave experiments at the continuum scale.

REFERENCES

Barker, L. M. and Hollenbach, R. E., 1970: Shock Wave Studies of PMMA, Fused Silica, and Sapphire, *J. Appl. Phys.* Vol. 44, 4208-4226.

Bourne, N. K., Green, W. H., and Dandekar, D. P, 2006: On the one-dimensional recovery and microstructural evaluation of shocked alumina, *Proc. of the Royal Soc. A.* published on line 2006 and references there in.

Chen, M.W., McCauley, J. W., Dandekar, D.P., and Bourne, N. K., 2006: Dynamic plasticity and failure of high-purity alumina under shock loading, *Nature Materials*. published on line July 2, 2006 and references therein.

Cooper, G. A., Millett, J. C. F., Bourne, N. K., and Dandekar, D. P., 2006: Delayed Failure in a Shock Loaded Alumina, *Shock Compression of Condensed Matter -2005,* Ed. M. D. Furnish, M. Elert, T. P. Russell, and C. T. White, American Institute of Physics, New York, 847-850 and references therein.

Dandekar, D. P. , 2001: Deformation of AD995 Alumina Under Repeated Plane Shock Wave Loading, *Impact Engineering and Applications*, Ed. A. Chiba, S. Tanimura and K, Hokamoto, Elsevier, New York, 785-790 and references therein.

Dandekar, D. P. and Bartkowski, P., 1994: Shock Response of AD995 Alumina, *High-Pressure Science and Technology-1993*, Ed. S. C. Schmidt, J. W. Shaner, G. A. Samara, and M. Ross, American Institute of Physics, New York, 733-736.

Ewart, L. and Dandekar, D. P.,1994: Relationship between the Shock Response and Micro-structural Features of Titanium Diboride *High-Pressure Science and Technology-1993*, Ed. S. C. Schmidt, J. W. Shaner, G. A. Samara, and M. Ross, American Institute of Physics, New York, 733-1201-1204.

Hirth, J. P. and Lothe, J., 1982: *Dislocation Theory* John Wiley & Son, Inc., New York, 2nd edition, 811-833.

Reinhart, W. D. and Chhabildas, L. C., 2003: Strength Properties of Coors AD995 Alumina in the Shocked State, *Int. J. Impact Eng*. 29, 601-609 and references there in.

NO. OF
COPIES ORGANIZATION

1 (PDF ONLY) DEFENSE TECHNICAL INFORMATION CTR
DTIC OCA
8725 JOHN J KINGMAN RD
STE 0944
FORT BELVOIR VA 22060-6218

1 US ARMY RSRCH DEV & ENGRG CMD
SYSTEMS OF SYSTEMS INTEGRATION
AMSRD SS T
6000 6TH ST STE 100
FORT BELVOIR VA 22060-5608

1 DIRECTOR
US ARMY RESEARCH LAB
IMNE ALC IMS
2800 POWDER MILL RD
ADELPHI MD 20783-1197

1 DIRECTOR
US ARMY RESEARCH LAB
AMSRD ARL CI OK TL
2800 POWDER MILL RD
ADELPHI MD 20783-1197

1 DIRECTOR
US ARMY RESEARCH LAB
AMSRD ARL CI OK T
2800 POWDER MILL RD
ADELPHI MD 20783-1197

ABERDEEN PROVING GROUND

1 DIR USARL
AMSRD ARL CI OK TP (BLDG 4600)

NO. OF COPIES ORGANIZATION

1 ODUSD (SANDT) WS
L SLOTER
ROSSLYN PLAZA N
STE 9030
1777 N KENT ST
ARLINGTON VA 22209-2210

1 COMMANDER
US ARMY MATERIEL CMD
AMXMI INT
9301 CHAPEK RD
FT BELVOIR VA 22060-5527

1 OFC OF NAVAL RSRCH
J CHRISTODOULOU
ONR CODE 332
800 N QUINCY ST
ARLINGTON VA 22217-5600

1 PEO GCS
SFAE GCS BCT/MS 325
M RYZYI
6501 ELEVEN MILE RD
WARREN MI 48397-5000

1 ABRAMS TESTING
SFAE GCSS W AB QT
J MORAN
6501 ELEVEN MILE RD
WARREN MI 48397-5000

1 COMMANDER
WATERVLIET ARSENAL
SMCWV QAE Q
B VANINA
BLDG 44
WATERVLIET NY 12189-4050

2 SFSJM CDL
AMMUNITION TEAM
R CRAWFORD
W HARRIS
1 ROCK ISLAND ARSENAL
ROCK ISLAND IL 61299-6000

2 COMMANDER
US ARMY AMCOM
AVIATION APPLIED TECH DIR
J SCHUCK
FT EUSTIS VA 23604-5577

NO. OF COPIES ORGANIZATION

1 NAVAL SURFACE WARFARE CTR
DAHLGREN DIV CODE G06
DAHLGREN VA 22448

1 USA SBCCOM PM SOLDIER SPT
AMSSB PM RSS A
J CONNORS
KANSAS ST
NATICK MA 01760-5057

3 AIR FORCE ARMAMENT LAB
AFATL DLJW
W COOK
D BELK
J FOSTER
EGLIN AFB FL 32542

1 DPTY ASSIST SCY FOR R&T
SARD TT
ASA (ACT)
J PARMENTOLA
THE PENTAGON RM 3E479
WASHINGTON DC 20310-0103

2 DARPA
W COBLENZ
L CHRISTODOULOU
3701 N FAIRFAX DR
ARLINGTON VA 22203-1714

1 US ARMY ARDEC
AMSTA AR AE WW
E BAKER
BLDG 3022
PICATINNY ARSENAL NJ
07806-5000

11 US ARMY TARDEC
AMSTRA TR R MS 263
K BISHNOI
D TEMPLETON (10 CPS)
WARREN MI 48397-5000

1 COMMANDER
US ARMY RSRCH OFC
A RAJENDRAN
PO BOX 12211
RSRCH TRIANGLE PARK NC
27709-2211

NO. OF COPIES ORGANIZATION

2 CALTECH
G RAVICHANDRAN
T AHRENS MS 252 21
1201 E CALIFORNIA BLVD
PASADENA CA 91125

5 SOUTHWEST RSRCH INST
C ANDERSON
K DANNEMANN
T HOLMQUIST
G JOHNSON
J WALKER
PO DRAWER 28510
SAN ANTONIO TX 78284

2 UNIV OF DELAWARE
DEPT OF MECH ENGR
J GILLESPIE
NEWARK DE 19716

3 SRI INTERNATIONAL
D CURRAN
D SHOCKEY
R KLOOP
333 RAVENSWOOD AVE
MENLO PARK CA 94025

1 APPLIED RSRCH ASSOCIATES
D GRADY
4300 SAN MATEO BLVD NE
STE A220
ALBUQUERQUE NM 87110

1 INTERNATIONAL RSRCH
ASSOCIATES INC
D ORPHAL
4450 BLACK AVE
PLEASANTON CA 94566

1 BOB SKAGGS CONSULTANT
S R SKAGGS
7 CAMINO DE LOS GARDUNOS
SANTA FE NM 87501

2 WASHINGTON ST UNIV
INST OF SHOCK PHYSICS
Y GUPTA
J ASAY
PULLMAN WA 99164-2814

NO. OF COPIES ORGANIZATION

1 COORS CERAMIC CO
T RILEY
600 NINTH ST
GOLDEN CO 80401

1 UNIV OF DAYTON
RSRCH INST
N BRAR
300 COLLEGE PARK
MS SPC 1911
DAYTON OH 45469-0168

2 COMMANDER
US ARMY TACOM
AMSTA TR S
T FURMANIAK
L PROKURAT FRANKS
WARREN MI 48397-5000

1 PROJECT MANAGER
ABRAMS TANK SYSTEM
J ROWE
WARREN MI 48397-5000

3 COMMANDER
US ARMY RSRCH OFC
B LAMATINA
D STEPP
W MULLINS
PO BOX 12211
RSRCH TRIANGLE PARK NC
27709-2211

1 NAVAL SURFACE WARFARE CTR
CARDEROCK DIVISION
R PETERSON
CODE 28
9500 MACARTHUR BLVD
WEST BETHESDA MD 20817-5700

4 LAWRENCE LIVERMORE NATL LAB
R GOGOLEWSKI L290
R LANDINGHAM L369
J E REAUGH L282
S DETERESA
PO BOX 808
LIVERMORE CA 94550

NO. OF COPIES ORGANIZATION

6 SANDIA NATL LAB
J ASAY MS 0548
R BRANNON MS 0820
L CHHABILDAS MS 0821
D CRAWFORD ORG 0821
M KIPP MS 0820
T VOLGER
PO BOX 5800
ALBUQUERQUE NM 87185-0820

3 RUTGERS
THE STATE UNIV OF NEW JERSEY
DEPT OF CRMCS & MATLS ENGRNG
R HABER
607 TAYLOR RD
PISCATAWAY NJ 08854

2 THE UNIVERSITY OF TEXAS
AT AUSTIN
S BLESS
IAT
3925 W BRAKER LN STE 400
AUSTIN TX 78759-5316

3 SOUTHWEST RSRCH INST
C ANDERSON
J RIEGEL
J WALKER
6220 CULEBRA RD
SAN ANTONIO TX 78238

1 CERCOM
R PALICKA
991 PARK CENTER DR
VISTA CA 92083

6 GDLS
W BURKE MZ436 21 24
G CAMPBELL MZ436 30 44
D DEBUSSCHER MZ436 20 29
J ERIDON MZ436 21 24
W HERMAN MZ435 01 24
S PENTESCU MZ436 21 24
38500 MOUND RD
STERLING HTS MI 48310-3200

1 INTERNATL RSRCH ASSN
D ORPHAL
4450 BLACK AVE
PLEASANTON CA 94566

NO. OF COPIES ORGANIZATION

1 JET PROPULSION LAB
IMPACT PHYSICS GROUP
M ADAMS
4800 OAK GROVE DR
PASADENA CA 91109-8099

3 OGARA HESS & EISENHARDT
G ALLEN
D MALONE
T RUSSELL
9113 LE SAINT DR
FAIRFIELD OH 45014

2 CERADYNE INC
M NORMANDIA
3169 REDHILL AVE
COSTA MESA CA 96626

3 JOHNS HOPKINS UNIV
DEPT OF MECH ENGRNG
K T RAMESH
3400 CHARLES ST
BALTIMORE MD 21218

2 SIMULA INC
V HORVATICH
V KELSEY
10016 51ST ST
PHOENIX AZ 85044

3 UNITED DEFENSE LP
E BRADY
R JENKINS
K STRITTMATTER
PO BOX 15512
YORK PA 17405-1512

10 NATL INST OF STANDARDS & TECH
CRMCS DIV
G QUINN
STOP 852
GAITHERSBURG MD 20899

2 DIR USARL
AMSRD ARL D
C CHABALOWSKI
V WEISS
2800 POWDER MILL RD
ADELPHI MD 20783-1197

NO. OF COPIES ORGANIZATION

ABERDEEN PROVING GROUND

66 DIR USARL
AMSRD ARL WM
S KARNA
J MCCAULEY (20 CPS)
J SMITH
T WRIGHT
AMSRD ARL WM B
J NEWILL
M ZOLTOSKI
AMSRD ARL WM M
S MCKNIGHT
R DOWDING
AMSRD ARL WM MC
R SQUILLACIOTI
AMSRD ARL WM MD
E CHIN
K CHO
G GAZONAS
J LASALVIA
P PATEL
J MONTGOMERY
J SANDS
AMSRD ARL WM T
P BAKER
B BURNS
AMSRD ARL WM TA
P BARTKOWSKI
M BURKINS
W GOOCH
D HACKBARTH
T HAVEL
C HOPPEL
E HORWATH
T JONES
M KEELE
D KLEPONIS
J RUNYEON
S SCHOENFELD
AMSRD ARL WM TC
R COATES
T FARRAND
K KIMSEY
L MAGNESS
S SEGLETES
D SCHEFFLER
R SUMMERS
W WALTERS

NO. OF COPIES ORGANIZATION

AMSRD ARL WM TD
T BJERKE
J CLAYTON
D DANDEKAR
M GREENFIELD
H MEYER
E RAPACKI
M SCHEIDLER
T WEERASOORIYA

NO. OF
COPIES ORGANIZATION

3 FRAUNHOFER-INSTITUT FÜR
KURZZEITDYNAMIK (EMI)
PROF DR K THOMA
DIPL-PHYS E STRAßBURGER
AM KLINGELBERG 1 D – 79588
EFRINGEN-KIRCHEN
GERMANY